

Research Paper

Spatial Distribution of Motor Endplates and its Adaptive Change in Skeletal Muscle

Xiaofeng Yin^{1*}, Tingting Yu^{2,3*}, Bo Chen¹, Jianyi Xu^{2,3}, Wentao Chen¹, Yisong Qi^{2,3}, Peixun Zhang¹, Yusha Li^{2,3}, Yuhui Kou¹, Yilin Ma^{2,3}, Na Han¹, Peng Wan^{2,3}, Qingming Luo^{2,3}, Dan Zhu^{2,3}, Baoguo Jiang¹

1. Department of Trauma and Orthopaedics, Peking University People's Hospital, Beijing 100044, China
2. Britton Chance Center for Biomedical Photonics, Wuhan National Laboratory for Optoelectronics, Huazhong University of Science and Technology, Wuhan 430074, China
3. MoE Key Laboratory for Biomedical Photonics, Collaborative Innovation Center for Biomedical Engineering, School of Engineering Sciences, Huazhong University of Science and Technology, Wuhan 430074, China

*These authors contributed equally to the manuscript.

✉ Corresponding authors: Prof. Baoguo Jiang, jiangbaoguo@vip.sina.com and Prof. Dan Zhu, dawnzh@mail.hust.edu.cn

© Ivyspring International Publisher. This is an open access article distributed under the terms of the Creative Commons Attribution (CC BY-NC) license (<https://creativecommons.org/licenses/by-nc/4.0/>). See <http://ivyspring.com/terms> for full terms and conditions.

Received: 2018.07.24; Accepted: 2018.12.22; Published: 2019.01.24

Abstract

Motor endplates (MEPs) are the important interfaces between peripheral nerves and muscle fibers. Investigation of the spatial distribution of MEPs could help us better understand neuromuscular functional activities and improve the diagnosis and therapy of related diseases.

Methods: Fluorescent α -bungarotoxin was injected to label the motor endplates in whole-mount skeletal muscles, and tissue optical clearing combined with light-sheet microscopy was used to investigate the spatial distribution of MEPs and in-muscle nerve branches in different skeletal muscles in wild-type and transgenic fluorescent mice. Electrophysiology was used to determine the relationship between the spatial distribution of MEPs and muscle function.

Results: The exact three-dimensional distribution of MEPs in whole skeletal muscles was first obtained. We found that the MEPs in the muscle were distributed in an organized pattern of lamella clusters, with no MEPs outside the lamella zone. Each MEP lamella was innervated by one independent in-muscle nerve branch and mediated an independent muscle subgroup contraction. Additionally, the MEPs changed along the lamella clusters after denervation and regained the initial pattern after reinnervation. The integrity and spatial distribution of MEPs could reflect the functional state of muscles. The signal absence of a certain MEP lamella could suggest a problem in certain part of the muscle.

Conclusions: The MEP lamella clusters might be the basis of neuromuscular function, and the spatial distribution of MEPs could serve as a testbed for evaluating the functional status of muscle and the therapeutic targeting map related to MEPs.

Key words: motor endplate, spatial distribution, α -bungarotoxin, optical clearing technique

Introduction

Motor endplates (MEPs) are important structural and functional interfaces between motor neurons and skeletal muscle fibers [1]. MEPs receive electrical signals from motor neurons, generate endplate potentials, and consequently induce muscle contractions [2]. The morphological structure of MEPs, especially their three-dimensional (3D) spatial

distribution in skeletal muscle, is closely related to the motor function of the muscle. In the study of peripheral nerve regeneration, on the one hand, to assess the regeneration and recovery of motor neurons, an intramuscular injection of a retrograde tracer dye is often used to label the motor neurons through the dye uptake by nerve terminals at the

MEP. The efficiency of labeling depends on whether the dye is located near the MEP. Due to the lack of spatial distribution of MEPs, there is a "blind" nature of intramuscular injection, which may lead to an underestimation of the number of motor neurons, thereby affecting the assessment efficacy [3, 4]. On the other hand, MEP degeneration after nerve injury is a hotspot in the field of peripheral nerve regeneration research, and most current research focuses on the changes of ultrastructure or local morphology of MEPs during injury and repair [5-7]. However, MEPs are not evenly distributed in skeletal muscles, and local structural information does not accurately reflect the condition of MEPs in overall skeletal muscles. Clinically, MEP is also a key target for the treatment of various diseases; for instance, an intramuscular injection of botulinum toxin type A can alleviate muscle spasms, and its efficacy depends on whether the injection site is near the MEP or the aggregation area [8-11]. Therefore, whether it is an in-depth understanding of the functional connection between nerves and muscles or research into nerve injury repair and clinical intervention, it is urgent to obtain the 3D spatial distribution of MEPs at the overall level of skeletal muscles.

There are several approaches to obtain the structures of MEPs. Some researchers use traditional immunohistochemical techniques [12-14], but only structural information of extremely thin muscle tissues, such as the diaphragm and the intercostal muscle, can be obtained; other researchers use acetylcholinesterase whole-muscle staining to observe the structure of MEP on the surface of a skeletal muscle [4, 13], but this method cannot provide the distribution information inside the skeletal muscle. There is also a method that combines traditional tissue sectioning, immunolabeling and computer simulation to reconstruct the 3D distribution of MEPs [3], but the entire process of slicing, mounting, labeling and imaging requires a large number of manual operations, which are both time-consuming and labor-intensive, followed by an extremely complicated image registration and data loss [15]. Overall, the structural information obtained by traditional methods is still in a fragmented state and cannot provide a sufficient scientific basis for the research and interventional treatment of nerve injury repair. Hence, there is an urgent need for new methods to obtain overall structural information of MEPs in skeletal muscles.

The development of various micro-optical imaging technologies provides important tools for high-resolution imaging of 3D structures of large tissues [16-20]. Traditional optical imaging technologies have limited imaging depth in biological tissues

and cannot meet the imaging needs of large tissues. For example, the depth of a confocal microscope is approximately 100-200 μm , and the imaging depth of a two-photon microscope is approximately 500-800 μm [16-18]. Light-sheet microscopy, developed in recent years, is a rapid imaging method that is suitable for imaging large tissues, but is only applicable to transparent samples [19, 20]. The imaging depth of these optical imaging techniques is limited by the high scattering properties of biological tissues.

The emergence of tissue optical clearing technology provides a new perspective for 3D imaging of large-volume tissues by introducing chemical agents and physical strategies to overcome the scattering of biological tissues [21-23]. The combination of tissue optical clearing and optical imaging provides an important means to acquire 3D images of tissue structures. In the past decade, various optical clearing methods have been developed, such as SeeDB [24], ScaleS [25], 3DISCO [26], CUBIC [27], and CLARITY [28], in addition to the corresponding series methods [29-35]. Most of tissue optical clearing methods were developed for brain, spinal cord or embryonic tissues and have not been reported in the study of skeletal muscle MEPs.

In this study, we aim to obtain 3D, structural information and spatial distributions of MEPs in different skeletal muscles based on the tissue optical clearing technique. First, we established a method to image MEPs in whole-mount skeletal muscles based on a modified MEP-labeling method and tissue optical clearing combined with light-sheet microscopy. Then, we obtained intact intramuscular MEPs in normal skeletal muscles and analyzed their spatial distribution pattern. Further, based on the nerve injury and repair model, we tracked the adaptive morphological and topological changes of MEPs. Finally, we explored the relationship between the spatial structure and muscle function by an electrophysiological examination. This work will help us better understand the structural and functional connections between nerves and muscles and hopefully provide a reference for research and clinical interventions related to nerve injury and repair.

Methods

Animals

Wild-type C57BL/6J mice (8-9 weeks old) were obtained from Beijing Vital River Laboratory Animal Technology Co., Ltd. (Beijing, China). Transgenic *Thy1-YFP-16*-line mice (8-9 weeks old) were obtained from Jackson Laboratory (Bar Harbor, Maine, USA). The experimental protocols were carried out in strict

accordance with the Chinese guidelines for the care and use of laboratory animals and were approved by the Animal Ethics Committee of Peking University People's Hospital (Beijing, China).

Animal models: denervated injury and tibial nerve repair

Wild-type C57BL/6J mice were anesthetized with isoflurane, and then the sciatic nerve and its main branches in the right limbs were exposed. The sciatic nerve was transected at 5 mm proximal to the bifurcation with a 3-mm-long nerve defect. The proximal and distal stumps were ligated with 5-0 nylon sutures separately and stitched to the adjacent muscles in reverse to prevent neural growth. For the tibial nerve repair model, the tibial nerve was transected at 3 mm distal to the bifurcation. Then the transected proximal and distal stumps were sutured with 12-0 nylon sutures by the "in situ epineurium suture" microsurgical technique [36]. The wound was closed with 5-0 nylon sutures. Picric acid was used to prevent toe self-biting behavior. Animals were raised with free access to food and water.

Labeling MEPs

Alexa Fluor 647-conjugated α -bungarotoxin (α -BTX 647) (Invitrogen, Carlsbad, California, USA) was injected via the tail vein to label MEPs. α -BTX 647 resulted in a lower background autofluorescence in muscles (i.e., a higher signal-to-noise ratio) than Alexa Fluor 594-conjugated α -bungarotoxin (α -BTX 594) (Invitrogen, Carlsbad, California, USA) (Figure S1). Hence, we used α -BTX 647 to label MEPs in this study. After injecting fluorescent α -BTX (0.3 μ g/g) via the tail vein with a 2-h conjugation time, the animals were perfused transcardially and the gastrocnemius was dissected. Then, 100 μ m tissue slices were made using a vibratome (Leica VT1000 S, Wetzlar, Germany). After imaging by confocal microscopy, the muscle slices were incubated in the α -BTX 647 solution (1:500 in phosphate-buffered saline, PBS) at room temperature for 30 min and then rinsed with 0.01 M PBS several times. After restaining, the slices were imaged again under the same confocal microscope. Additionally, to validate the labeling of acetylcholine receptors (AChRs) of MEPs in denervated muscles, we imaged the labeled and unlabeled gastrocnemius muscles after one-month denervation by ultramicroscopy. The unlabeled muscle did not present any bright spots with strong signals, indicating that nothing looking like MEP was present before BTX labeling.

Electrophysiological examination

To assess the labeling efficiency of fluorescent α -BTX, electrophysiological examination was

conducted at 0, 15, 30, 60, 90, and 120 min after injecting α -BTX 647. Following anesthesia, the sciatic nerve and its main branches were exposed. The stimulating electrode was placed at 0.5 cm proximal to the bifurcation. The recording electrodes were placed in the gastrocnemius muscle, while the ground electrode was placed in the subcutaneous tissue. Rectangular pulses (duration: 0.1 ms; intensity: 0.06 mA; frequency: 5 pulses per second) were used (Medlec Synergy, Oxford Instrument Inc., Oxford, UK), and the compound muscle action potentials (CMAPs) in the gastrocnemius were recorded. α -BTX is a selective antagonist of AChRs that induces decreased CMAPs. Hence, the labeling efficiency was judged by the amplitude decrease of the CMAPs.

To further validate the functional relationship of in-muscle nerve branches to muscle contraction based on structural lamella clusters, rectangular pulses (duration: 0.1 ms; intensity: 0.06 mA; frequency: 100 pulses per second) were used to induce tetanic contraction, which was used to judge the responses of each gastrocnemius subgroup to the electrical stimulation on the corresponding nerve branch.

Perfusion and sample preparation

Animals were anesthetized with a mixture of 2% chloral hydrate and 10% urethane through intraperitoneal injection and perfused transcardially with 0.01 M PBS followed by 4% paraformaldehyde. The gastrocnemius, tibialis anterior, quadriceps, biceps brachii, and triceps brachii were dissected and post-fixed overnight at 4 °C in 4% paraformaldehyde. Then, the muscles were rinsed with PBS several times. To investigate the influence of the optical clearing technique on the samples' fluorescence, the gastrocnemius was sliced into 100 μ m cross-sections with a vibratome. For the denervation model, the muscles were excised at 1 week, 2 weeks, 1 month, 2 months, 3 months, and 6 months after operation. For the tibial repair model, the mice were sacrificed at 1 year after operation and processed in the same way.

Labeling of muscle fibers

The dissected and post-fixed muscles, including gastrocnemius, tibialis anterior, quadriceps, biceps brachii, and triceps brachii, were cut from the mid-belly of the fixed muscles and rinsed in water for 12 h. After that, the samples were dehydrated in 50%, 70%, 80%, 95% and 100% ethanol solutions (each for 30 min), immersed in xylene twice (each for 12 min) and embedded in paraffin. Then, the samples were cut into 4- μ m-thick cross-sections by a microtome (RM2016, Leica, Wetzlar, Germany) and stained with hematoxylin and eosin (H&E). Following H&E staining, the cross-sections were imaged with a microscope

(NIKON CI-S, NIKON, Tokyo, Japan) equipped with a color digital camera (DS-Fi2, NIKON, Tokyo, Japan). The obtained images were viewed with the NDP.view 2.3.1 software (Hamamatsu Dentist Databases Records, Hamamatsu, Japan) and the number of the muscle fibers on each H&E-stained cross-section was counted manually by an independent researcher.

Tissue optical clearing

For most of the muscles, we used a typical clearing method, called 3DISCO, for clearing. First, tetrahydrofuran (Sinopharm Chemical Reagent Co., Ltd, Shanghai, China) and dibenzyl ether (Sigma-Aldrich, St. Louis, USA) were preprocessed with basic activated aluminum oxide (Sigma-Aldrich, St. Louis, USA) to remove the residual peroxides. Then, the fixed muscle samples were incubated with 50%, 70%, 80%, and 100% tetrahydrofuran for dehydration, each for 2-3 h (30 min for muscle slices) in glass vials while gently shaking. After that, the samples were placed into dibenzyl ether until they became completely transparent. For the muscles from *Thy1-YFP-16* mice, an optimized method, called FDISCO, was used [35]. For the other clearing methods, including FRUIT, SeeDB, ScaleS, and CUBIC (Figure S2), the clearing protocols were performed following the original publications [24, 25, 27, 29].

Laser-scanning confocal microscopy

Before and after clearing, muscle slices were mounted with two cover glasses and imaged with an inverted confocal fluorescence microscope (LSM710, Zeiss, Oberkochen, Germany) equipped with the Fluar 10×/0.5 objective (dry, working distance: 2.0 mm) and Plan-Apochromat 20×/0.8 objective (dry, working distance: 0.55 mm).

Ultramicroscopy

The UltraMicroscope I (LaVision BioTec, Bielefeld, Germany), equipped with 2×/0.5 objective (dry, working distance: 20 mm), was used to image the cleared intact muscles. This instrument could create a thin light-sheet to illuminate the cleared biological samples while imaging perpendicular to the light-sheet. For the AChRs labeled with α -BTX 647 or α -BTX 594, 633 nm or 561 nm was applied as the exciting wavelength, respectively. The z step size was set to 5 μ m. After setting the imaging parameters appropriately, images of the samples were acquired for subsequent processing and analysis.

Data processing and quantification

Image processing was executed using a Dell workstation with an 8-core Xeon processor, 128 GB RAM and an AMD Radeon HD 7900 Series graphics card. The obtained bright-field and fluorescent images

were analyzed with ImageJ (National Institutes of Health, Bethesda, Maryland, USA) and Imaris software (Bitplane, Zurich, Switzerland). The 3D visualization and quantification were performed via the Spots, Surfaces and Filaments modules in Imaris. Quantification graphs were drawn using MATLAB, Microsoft Excel, or GraphPad Prism.

Fluorescence was quantified with the freehand-selection tool in ImageJ. For the characteristic measurement of muscles, maximum-intensity projections of z stacks were made with ImageJ, and the Straight Line tool was used to measure the maximum diameter. For the measurement of band width of MEPs' lamella clusters, the reconstructed data of intact gastrocnemius were resampled in the cross-section, and maximum-intensity projections of z stacks (thickness = 200 μ m) were made with ImageJ (Figure 4A). The width was measured perpendicular to the direction of the trend line of each band while taking into account the uneven distribution of each band. Five to ten positions in each band were measured (Figure S3), and the maximum value of each band was used for averaging to calculate the band width of the MEPs. For the evaluation of linear deformation, the unclarified and cleared muscles were put in a glass dish filled with PBS or clearing solution and photographed with a camera on grid paper. Transmission and reflection images were taken for each muscle. Based on top-view photos, the lines parallel and perpendicular to the muscle fibers were determined with ImageJ. The linear deformations after clearing in these two directions were quantified by normalizing the value to that before clearing. All the relative data in this paper were calibrated with the corresponding shrinkage ratio. Based on the automated calculation and segmentation of Imaris, we also modified the segmentation results with manual selection or cutting based on artificial judgment to distinguish two MEPs that were too close or to eliminate incorrect data points, such as the background point with strong intensity from the residual bubbles in samples after clearing and the autofluorescence from muscle fibers.

Statistical analysis

GraphPad Prism5 was used for statistical analysis. The one-sample *t*-test was used in Figure 1G. One-way ANOVA was used to compare the differences between more than two groups. If ANOVA results were significant, the Dunnett's post hoc test for multiple comparisons was conducted (Figure 3B, D). The paired *t*-test was used to compare samples' shrinkage data between fiber direction and the perpendicular direction (Figure S4B). In Figure 3F, the non-parametric test (Kruskal-Wallis test) was conducted based on a non-normal distribution.

Results

Labeling and optical clearing for 3D imaging of MEPs in un-sectioned skeletal muscles

To label the AChRs on the postsynaptic membrane of MEPs in un-sectioned skeletal muscles, α -BTX 647 was injected into the tail vein of wild-type C57BL/6J mice. Electrophysiological examination showed that the amplitude of the CMAP in the gastrocnemius was reduced by 82% at 60 min after injecting α -BTX 647, which indicated that more than 80% of the MEPs were blocked and labeled (Figure 1A). At 120 min after injecting α -BTX 647, almost no

CMAP was induced, indicating that almost all of the MEPs were labeled. The specific fluorescence signal of MEPs could be observed clearly at 120 min after injecting α -BTX 647. To corroborate the high labeling efficiency of the MEPs, we relabeled the muscle slices through a traditional incubation in α -BTX 647 solutions after *in vivo* injection (Figure 1B-C). The results indicated almost complete labeling of MEPs, with no significant difference in the MEP counts before and after relabeling. This technique, therefore, provided a simple and highly efficient method for the uniform labeling of MEPs in skeletal muscles.

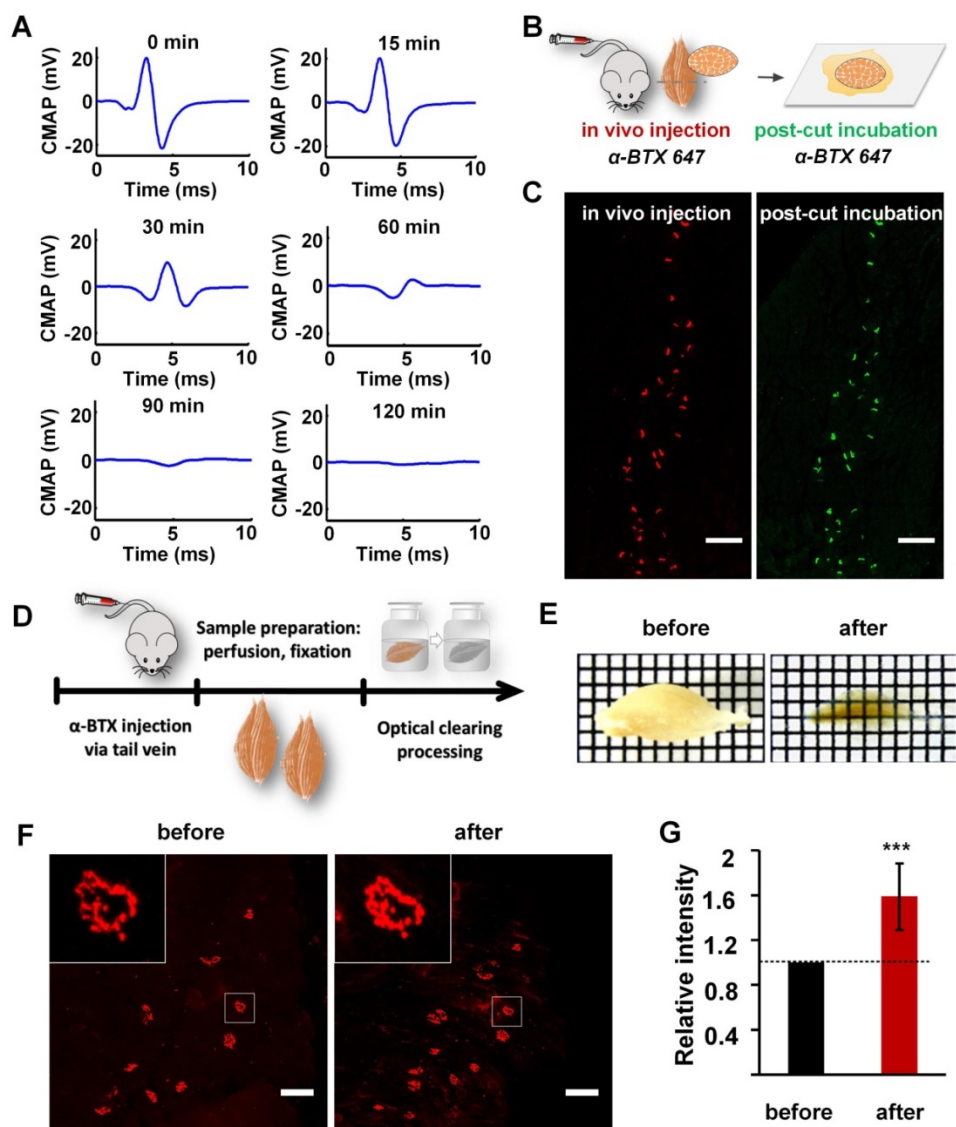


Figure 1. Labeling and clearing of skeletal muscles. (A) Electrophysiological examination by electrical stimulation on the sciatic nerve at 0 min, 15 min, 30 min, 60 min, 90 min, and 120 min after injecting α -BTX 647 via the tail vein. The amplitude of the CMAP in the gastrocnemius was reduced by over 80% at 60 min after injecting α -BTX 647, and nearly no CMAP was induced in the gastrocnemius at 120 min. (B) Schematic diagrams illustrating MEP labeling by the *in vivo* injection of α -BTX, and post-cut restaining of the same muscle slices by traditionally incubating in α -BTX 647 solution for 30 min. Notably, α -BTX 647 was a better choice due to the lower background autofluorescence compared to α -BTX 594 (Figure S1). (C) MEPs in the cross-section (100 μ m) of the gastrocnemius labeled by an *in vivo* injection (red) and post-cut restaining using the traditional incubation method (green). Pseudo-colors are used in the images, and both pre- and post-cut labeling were done with the same α -BTX 647. Scale bar: 200 μ m. (D) Diagram of sample processing. (E) Transparency of the gastrocnemius before and after 3DISCO clearing. Grid size: 1.45 mm \times 1.45 mm. (F) Confocal images of MEPs labeled with α -BTX 647 before and after 3DISCO clearing. Insets are the enlarged images indicated by the white frame. Scale bar: 100 μ m. (G) Fluorescence quantification. The intensities of fluorescence before and after clearing were both measured ($n = 10$). The relative fluorescence intensity was calculated by dividing the intensity after clearing by the value before clearing. Hence, the relative intensity before clearing is 1, and the data after clearing are presented as the mean \pm s.d. The fluorescence intensity shows a significant increase after clearing. (One-sample t-test; *** $P < 0.001$).

Optical clearing techniques provide a powerful tool for 3D mapping of large-volume biological samples. We compared the transparency of gastrocnemius sample cleared with FRUIT, SeeDB, ScaleS, CUBIC, and 3DISCO, and found that 3DISCO presented the best clearing capability on samples (Figure S2). As shown in Figure 1D-E, after clearing with 3DISCO, the muscle showed good transparency with a clear grid background. As a critical factor for deep-tissue imaging, fluorescence preservation was also investigated. Confocal imaging under the same parameters showed that there was no obvious decrease in the fluorescence signal intensity of α -BTX 647-labeled MEPs (Figure 1F). Further fluorescence quantification revealed that the mean fluorescence intensity increased significantly after clearing (Figure 1G), which might have been due to the shrinkage of muscle samples (Figure S4). These results indicate that the 3DISCO protocol can achieve good

transparency of skeletal muscles and fluorescence preservation of fluorescent α -BTX, and the combination of *in vivo* injection of α -BTX 647 and 3DISCO can be used for the clearing and imaging of mouse muscle samples.

The distribution pattern of MEPs in skeletal muscles

In vivo injection of fluorescent α -BTX as well as the 3DISCO protocol were combined with ultramicroscopy to further determine the 3D distributions of MEPs in different skeletal muscles, including gastrocnemius, tibialis anterior, quadriceps femoris, biceps brachii and triceps brachii. Our results showed that the MEPs were distributed in lamella clusters (Videos S1-5). Each skeletal muscle had distinctive patterned lamella clusters (Figure 2 and Figure S5). The distribution of the lamella clusters in the tibialis anterior and quadriceps femoris resembled

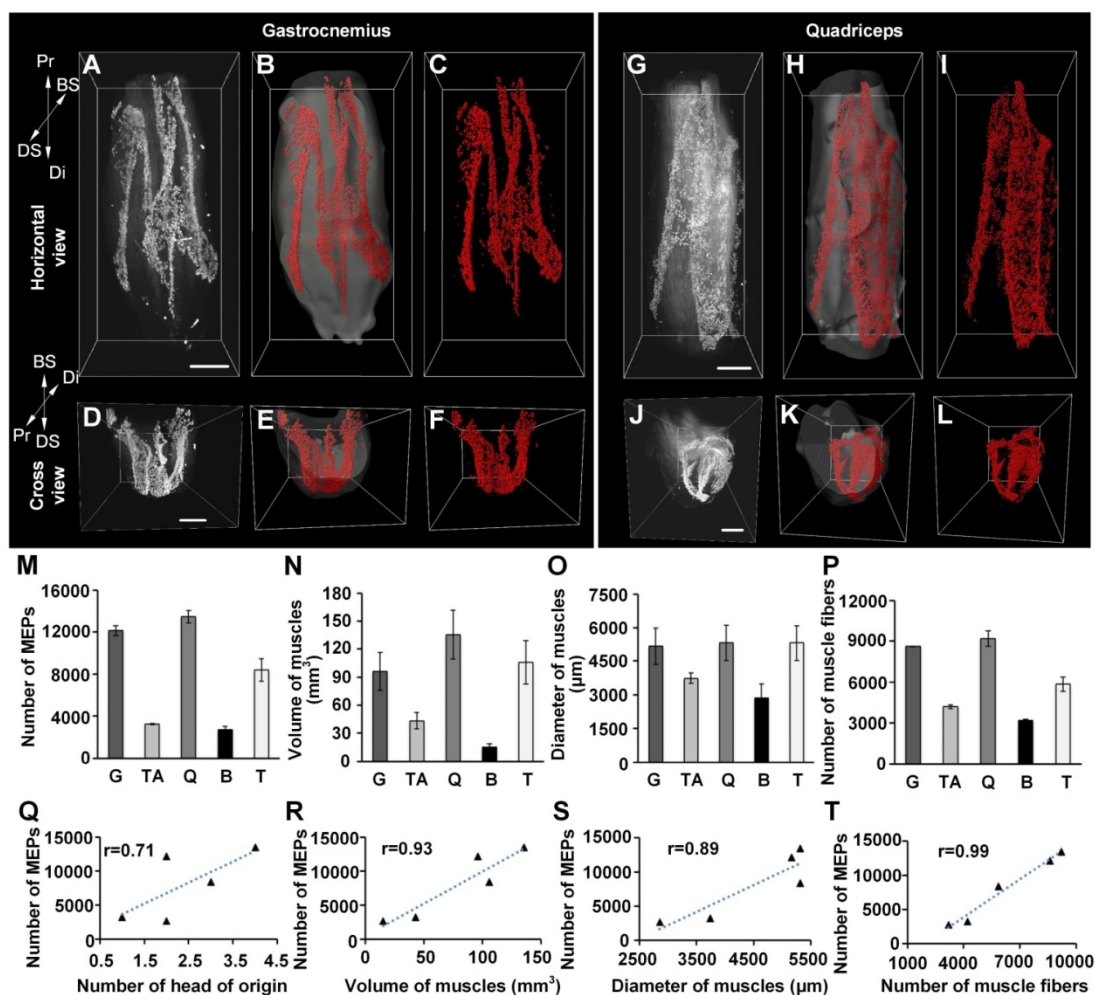


Figure 2. Three-dimensional distributions of MEPs in different skeletal muscles. (A-L) Three-dimensional reconstruction of MEPs in the gastrocnemius and quadriceps. A and G show the horizontal view of raw image stacks (white). B and H show the segmentation of muscle surfaces (light gray) and MEPs (red). C and I show the MEPs (red). D, E, F, J, K, and L reveal the cross-sectional view corresponding to A, B, C, G, H, and I. Three-dimensional reconstructions of the tibialis anterior, biceps, and triceps are shown in Figure S5. BS: bone surface; Di: distal end; DS: dorsal surface; Pr: proximal end. Scale bar: 1000 μ m. (M-P) The statistical results of different muscles ($n = 3$ for each muscle): the total number of MEPs (M), volume (N), maximum diameter (O), and number of muscle fibers (P). B: biceps; G: gastrocnemius; Q: quadriceps; T: triceps; TA: tibialis anterior. Data are presented as the mean \pm s.d. (Q-T) The correlation analysis between the number of MEPs and each of the following parameters: the number of the head of origins (Q), volume (R), diameter (S), and fiber number (T) of muscles.

a “bougainvillea” (Figure S5A-F) and “calla lily” (Figure 2G-L), respectively. For the triceps brachii and gastrocnemius muscle, the distribution of the lamella clusters resembled a check mark (i.e. “✓”) (Figure S5M-R) and the capital letter “M” (Figure 2A-F), respectively. The lamella clusters were parallel in the biceps brachii, with one broad triangle-like lamella cluster and one narrow stripe-like lamella cluster (Figure S5G-L).

Moreover, we counted the MEPs in each muscle. The results demonstrated obviously different values among the muscles. To examine the relationship between the number of MEPs and the morphologic parameter of the muscles, we further measured the volume, maximum diameter, and fiber number of different muscles and recorded the heads of origins (Figure 2M-P). The correlation analysis between the number of MEPs and each morphologic parameter showed that the number of MEPs was highly correlated with the number of muscle fibers, muscle volume and muscle diameter (Figure 2Q-T), which means that a greater fiber number, muscle volume, or diameter was associated with a greater number of MEPs. Taking gastrocnemius as an example, the mean width of the lamella clusters was $138 \pm 16 \mu\text{m}$, and the mean area of the maximum-intensity projection (MIP) of the lamella clusters was $(38.8 \pm 7.0) \times 10^4 \mu\text{m}^2$, occupying $3.6 \pm 0.4\%$ of the largest cross-section in the gastrocnemius.

The adaptive changes of MEPs in skeletal muscles after peripheral nerve injury and repair

To investigate the adaptive changes to MEPs after muscle denervation, the muscle atrophy and the anatomical characteristics of MEPs were investigated in the denervated model with the sciatic nerve transected (Figure 3A). The weight of the denervated gastrocnemius decreased from $0.18 \pm 0.02 \text{ g}$ to $0.06 \pm 0.01 \text{ g}$ at 6 months after denervation (Figure 3B). The mean width of the lamella clusters was increased from $138 \pm 16 \mu\text{m}$ to $368 \pm 50 \mu\text{m}$ at 2 months after denervation, with a significant decrease in the mean volume of single MEP (Figure 3C-F). The number of MEPs (or MEP fragments) increased from 12886 ± 266 to 15506 ± 306 during the first month after denervation, then decreased to 447 ± 114 at 6 months after denervation (Figure 3E). Our results suggest that the AChRs in MEPs stained by α -BTX were disintegrated and fragmented along the lamella clusters after denervation until they completely disappeared (Video S12). In addition, after one-year recovery in the tibial nerve repair model, the gastrocnemius regained its patterned distribution of the lamella clusters (Figure S6). These results indicate

that the gastrocnemius lost or regained neuromuscular function on the basis of the MEP lamella clusters.

Relationship between the distribution of MEPs and muscle function

Based on fundamental knowledge of traditional anatomy, the gastrocnemius can be divided into the medial head and the lateral head. However, the lateral head can be further divided into three subparts according to the distribution of the MEP lamellas. Figure 4 and Table 1 show the structural composition and electrophysiological characteristics of the different components of MEP lamellas, respectively.

Table 1. Electromyography of gastrocnemius in mice.

	Tibial nerve trunk	MNB	LNB1	LNB2+LNB3	LNB2+LNB3 (with LNB3 transected)
MML			-	-	-
LML1		-		-	-
LML2		-	-		
LML3		-	-		-

When stimulating the MNB, LNB1, LNB2, and LNB3 separately, an independent compound muscle action potential and muscle contraction was induced in the area of medial MEP lamella (MML), lateral MEP lamella 1 (LML1), LML2, and LML3, respectively.

MML: medial MEP lamella; MNB: medial nerve branch; LML1: lateral MEP lamella 1; LNB1: lateral nerve branch 1; LML2: lateral MEP lamella 2; LNB2: lateral nerve branch 2; LML3: lateral MEP lamella 3; LNB3: lateral nerve branch 3.

The observation that MEPs were distributed in distinct lamella clusters in skeletal muscles suggested that there might be a functional relationship between the distribution pattern and muscle function. Thus, we analyzed the innervation pattern of lamella clusters in the gastrocnemius by imaging the branches of the tibial nerve using a specific fluorescent protein (YFP) signal (from *Thy1-YFP-16* mice) and MEPs through the *in vivo* injection of α -BTX 647. We found that the gastrocnemius had four lamella clusters, with one or more in-muscle nerve branches in each lamella cluster (Figure 4 and Video S6). Moreover, the other skeletal muscles revealed similar lamella cluster-like characteristics with one or more in-muscle nerve branches, such as tibialis anterior (Video S7), quadriceps (Video S8), biceps (Video S9) and triceps (Video S10). This phenomenon suggested that for each lamella cluster, the corresponding nerve branches and innervated muscle fibers might be a distinctive structural and functional unit. Further, we conducted electrophysiological examination in mouse gastrocnemius and found that when stimulating each in-muscle branch of the tibial nerve as indicated in the gross anatomy of the gastrocnemius (Figure 4E), including the medial nerve branch (MNB), lateral nerve branch 1 (LNB1), lateral nerve branch 2 (LNB2), and lateral nerve branch 3 (LNB3), an independent CMAP and muscle subgroup contraction could be

recorded at each branch corresponding to the MEP lamella cluster (Table 1 and Video S11). Thus, the gastrocnemius probably consists of four functional units based on the distribution of the MEPs, each of which consists of one lamella cluster formed by MEPs, the corresponding nerve branches and the innervated

muscle fibers (Figure 4E). The integrity and distribution of MEPs could reflect the functional state of muscles. The signal absence of a certain MEP lamella could suggest a problem in certain part of the muscle.

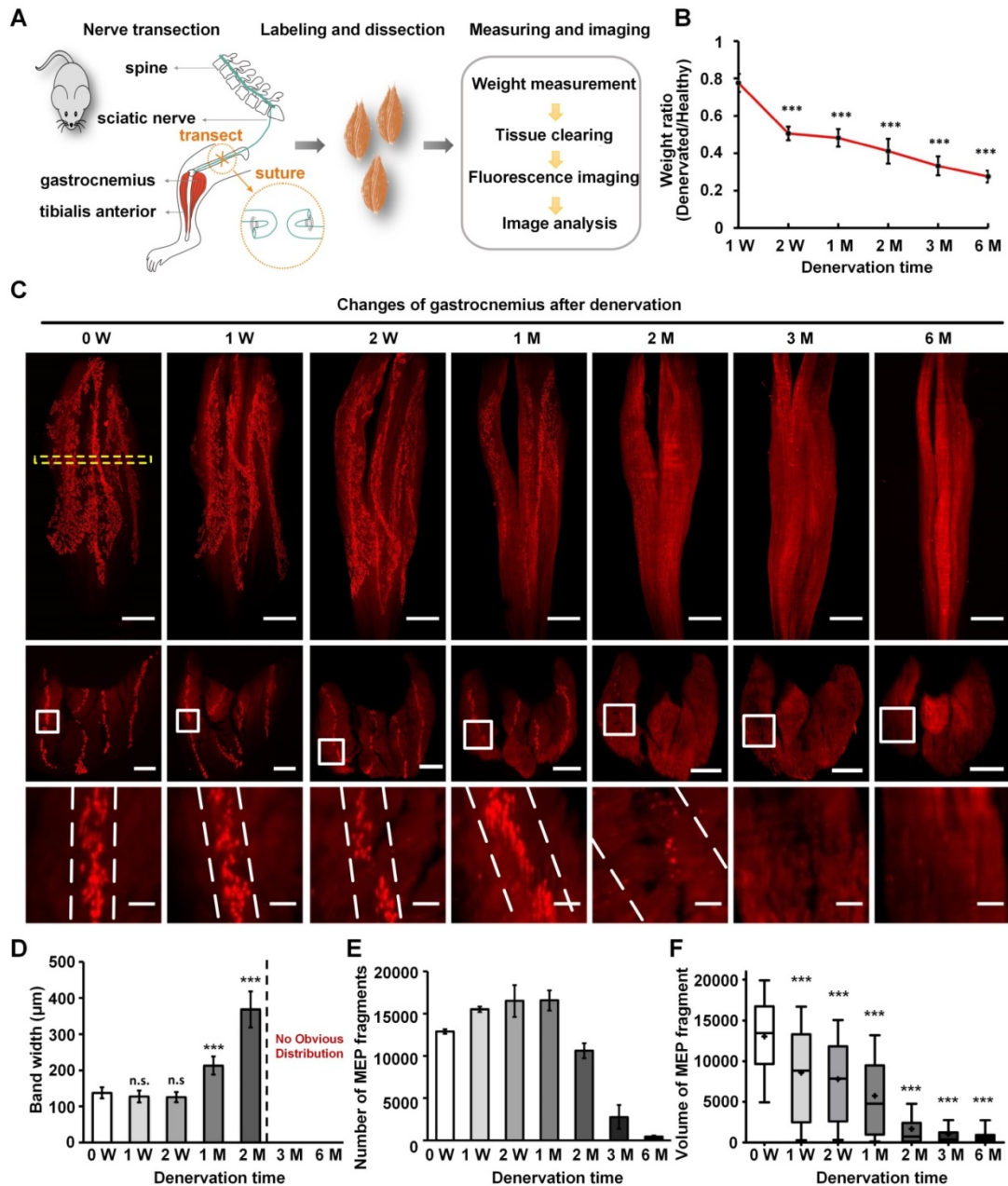


Figure 3. Characteristics of MEPs in the denervated gastrocnemius muscles over time. (A) A schematic diagram of the denervated mouse model. (B) Weight of the denervated gastrocnemius relative to healthy muscle. The weight ratio at 2 weeks (W), 1 month (M), 2 M, 3 M, and 6 M after denervation was significantly different from that at 1 W. $***P < 0.001$ (one-way ANOVA). Data are presented as the mean \pm s.d. (C) Spatial conformation of AChRs stained by α -BTX in MEPs at different time points (0 W, 1 W, 2 W, 1 M, 2 M, 3 M, and 6 M) after denervation. The cross-sectional images in the second row are maximum projections of z stacks (thickness = 250 μ m), which are located at the position similar to 0 W, indicated with the yellow dotted box. The enlarged images indicated by white frames are shown in the third row. The scale bars represent 1000 μ m for the first row, 500 μ m for the second row, and 100 μ m for the third row. (D) Band width of the lamella clusters ($n = 3, 4, 6, 6, 6$ mice for 0 W, 1 W, 2 W, 1 M, 2 M, respectively). n.s.: not significant; $**0.001 < P < 0.01$; $***P < 0.001$ (one-way ANOVA followed by Dunnett's post hoc test) compared with 0 W. Note that there were no obvious MEP lamella clusters at 3 M and 6 M in (C); thus, we could not measure the data. (E) The total number of AChR-concentrated fragments in MEPs with the varying denervation times ($n = 3, 4, 6, 6, 5, 6$ for 0 W, 1 W, 2 W, 1 M, 2 M, 3 M, 6 M, respectively). Data are presented as the mean \pm s.d. (F) Box plots of the volume of a single AChR-concentrated fragment in MEP. Bars indicate the 10th and 90th percentiles. Statistical significance was assessed by the Kruskal-Wallis test. $***P < 0.001$, compared with 0 W.

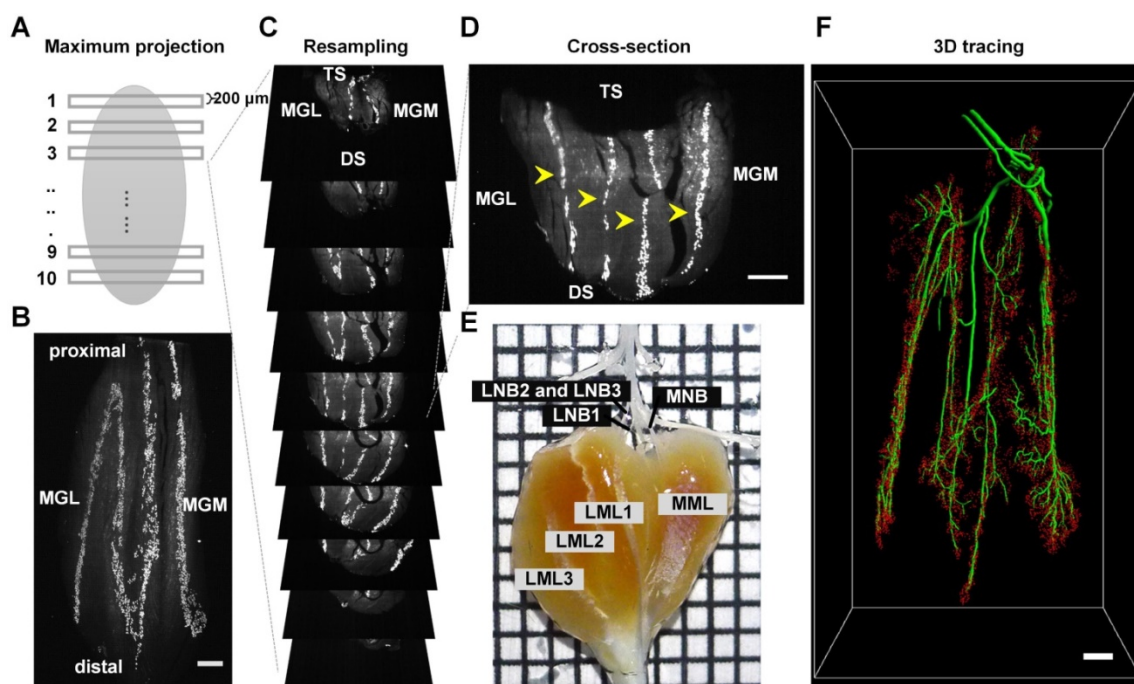


Figure 4. Distribution of MEPs and the innervation pattern of the gastrocnemius. (A) A schematic diagram of the MIP of the cross-section. (B) MIP of the horizontal-section (thickness = 600 μm). MGL: gastrocnemius lateralis; MGM: gastrocnemius medialis. (C) Resampling cross-sections of the intact gastrocnemius. DS: dorsal surface; TS: tibial surface. (D) Lamella clusters of MEPs in cross-section (thickness = 200 μm) indicated with yellow arrowheads. (E) Gross anatomy of the gastrocnemius and its innervating nerve branches. The gastrocnemius consists of four functional units based on the distribution of MEP lamellas, which are innervated by the medial nerve branch (MNB), the lateral nerve branch 1 (LNB1), the lateral nerve branch 2 (LNB2) and the lateral nerve branch 3 (LNB3), respectively. Grid size: 1.45 mm × 1.45 mm. (F) Segmentation of MEPs (red) and tracing of the nerve branches (green). Scale bar: 500 μm.

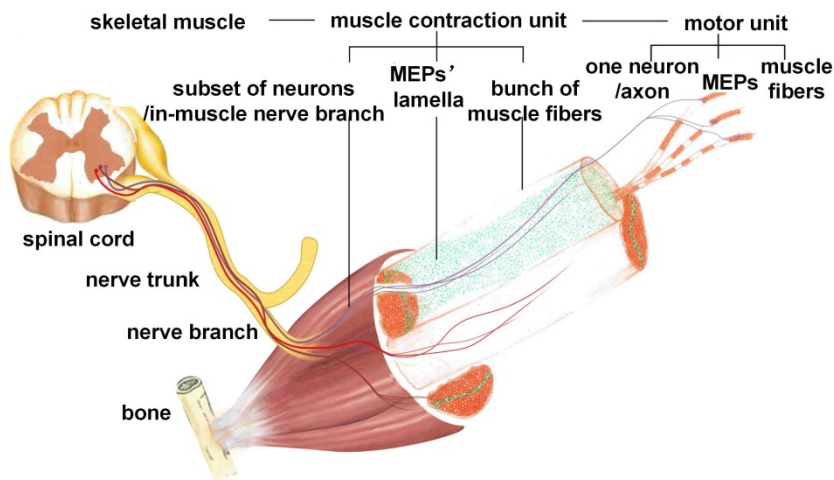


Figure 5. Schematic diagram of the functional group based on MEP lamella distribution. Each functional group is formed by one MEP lamella cluster, the corresponding in-muscle nerve branches, and the innervated muscle fibers.

Discussion

The spatial distribution of MEPs in whole skeletal muscles was obtained in this study. To find the distributions of MEPs in un-sectioned mouse skeletal muscles, a novel and convenient method combining *in vivo* injection of fluorescent α-BTX with optical clearing and ultramicroscopy was utilized here. As an antagonist of AChR, α-BTX selectively binds to AChRs on the postsynaptic membrane, blocks transmitters' transmission at the MEPs, and prevents muscle contractions [37]. Fluorescent α-BTX

can be transported to label the whole skeletal muscle's MEPs easily through blood circulation after injection via the tail vein [38]. According to our electrophysiological and post-cut restraining results, most of the MEPs were labeled. This labeling method avoids the common problems associated with traditional histological methods [3, 39], which are laborious and time-consuming. After clearing with 3DISCO, we imaged different muscles with ultramicroscopy and obtained 3D structures by serial optical sectioning with a thin light-sheet (thickness: 5-10 μm). This could also eliminate the large defects

and the loss of information associated with traditional histologic sectioning and imaging [20, 40, 41], facilitating subsequent 3D reconstruction. In summary, the clearing method combined with light-sheet microscopy provides a new and convenient tool to investigate the characteristics of MEPs in un-sectioned skeletal muscles, such as the distribution, number, and volume of MEPs.

Our results revealed that the MEPs in mouse skeletal muscles were distributed in an organized pattern of lamella clusters. The MEPs were concentrated around thin-layer areas (i.e., lamella clusters) in skeletal muscles. Almost no MEPs were outside of the lamella clusters. MEP lamella clusters were embedded in a stretched- or curled-layer-like pattern in the muscles, with one or more corresponding in-muscle nerve branches. As shown in **Figure 5**, a peripheral nerve trunk has several branches. When the nerve penetrates into the muscle, it sends out several in-muscle nerve branches, each of which corresponds to one MEP lamella cluster. Each MEP lamella cluster is the interface between the ending network of the in-muscle nerve branch and muscle fibers, and submaximal contractions of gastrocnemius or other muscles are due to the recruitment of a number of motor units from different lamella clusters rather than to the synchronous activity of motor units within the same cluster. Thus, a muscle can be divided into several subgroups according to the distribution of the MEP lamellas. The number, volume, and distribution of MEP lamellas constitute the ties between nerve innervation and muscle function, determining the fine movement of skeletal muscles. Previous studies also described bands or columns of MEPs in human skeletal muscles. Coers and Durand observed, in longitudinal sections of whole muscles of three infant cadavers, that the MEPs were always situated at the midpoint of the muscle fibers and were concentrated in narrow zones [42]. Christensen examined muscles from stillborn infants and confirmed that, in the unipennate muscles, the MEPs formed a transverse band through the middle of the muscle and, in the bipennate muscles, there was a concave endplate band [43]. Their findings are in agreement with ours. In this work, we mapped all MEPs in each muscle combining *in vivo* BTX staining, tissue clearing technique and light-sheet microscopy, which allowed the visualization and quantification of the 3D distribution of the MEPs in the intact muscle. The findings here give us a more intuitive way to understand the organization and contraction mechanism of a skeletal muscle. It will enrich our understanding of skeletal muscle movements and the complex and coordinated motion of the body. The adaptive changes of MEPs

after denervation or reinnervation also progressed in the organized pattern of lamella clusters. During denervation, the MEPs changed along the lamella clusters, with an increased mean width of the lamella cluster and a seemingly decreased mean volume of a single MEP fragment. As shown in **Figure 3** and **Figure S7**, the AChRs on the postsynaptic membrane, which were stained by α -BTX, disintegrated to form small fragments. These fragments then spread over time and eventually disappeared completely. The increase in the fluorescence counting does not mean an increase in single MEPs, but reflects the process of disintegration of the MEPs. While the AChR-concentrated areas in MEPs were broken down into several small fragments and scattered, it looks like the band was broadening (**Figure 3C**). Such alterations in AChR density at the neuromuscular junction were also reported by Akaaboune et al [44]. Furthermore, we observed the pathological changes of MEPs following nerve repair and found that the gastrocnemius regained its "M"-like patterned lamella clusters of MEPs. All of these results revealed that the lamella cluster-like pattern of MEPs was the basis of neuromuscular function. However, the regained MEP organization did not mean the complete recovery of muscle function. It also involved changes in the composition and distribution of motor units, signal transference in neuromuscular junctions, and changes in muscle fibers after nerve injury. There are different types of motor units in the muscles, and the muscle fibers of each motor unit are scattered over relatively large areas of the muscle, with motor unit fields largely overlapping [45, 46]. In contrast, as shown in another study [47], motor units in reinnervated muscles occupy a considerably smaller area than normal (approximately one-third), despite the fact that they contain a similar mean number of fibers, thereby accounting for the type grouping observed by histochemistry in reinnervated muscles. This means that, although the anatomical organization of MEPs is apparently "regained" after reinnervation, the neuromuscular connections are altered, which explains the alterations of motor unit action currents in neurogenic lesions. Despite this, the distribution of MEPs could still be used as a reference to judge the status of muscle function.

Based on these results, one skeletal muscle could be divided into one or several functional groups, mainly according to the distribution of the MEP lamella clusters. Each functional group consists of all MEPs in one lamella cluster, the corresponding nerve branches and the innervated muscle fibers. Such a functional group receives electrical signals and induces muscle subgroup contraction. Electrophysiological examination also indicated that an

independent muscle subgroup contraction could be induced when electrically stimulating each in-muscle nerve branch, which suggested that each functional group in gastrocnemius had an independent pathway of neuromuscular signal transmission. As the MEP is the interface between peripheral nerves and muscle fibers, the concentration of MEPs in the middle of the muscle fiber may contribute to the synchronous signal transference from the nerve ending to the muscle fibers. The contraction order from the neurons connected to the same cluster of MEPs will arrive to the muscle fibers and lead to actions of all involved fibers at the same time to cause the fine movement of the muscle. One muscle or one head of a muscle in traditional anatomy can, thus, be divided into more separate subunits and lead to a more precise movement of the muscle. The electrical signal changes and spatial locations of such functional groups could be used as novel diagnostic clues for disease diagnosis or treatment.

In summary, the 3D images of un-sectioned mouse skeletal muscles were first obtained by combining tail vein injection of fluorescent α -BTX *in vivo* with the optical clearing technique and ultramicroscopy. The distribution of the MEP lamella clusters and results from electrophysiological examination will allow a better understanding of the detailed working pattern in skeletal muscle contraction and more exact descriptions of the pathological changes following peripheral nerve injury or other neuromuscular diseases. Clinically, surgeons should learn more about the distributions of the MEPs in the muscles and try their best to avoid or reduce injuries to peripheral nerves and MEP lamella clusters to maintain maximum muscle function [48-50]. In other words, during operations, surgeons should not only pay attention in choosing muscle gap as a surgical approach but also avoid destroying an MEP lamella, choosing the interlamellar approach. Additionally, the distribution of MEPs could help physicians to more precisely detect in-muscle nerve branch injury, which could be easily omitted by traditional electromyography. Muscles can be subdivided into more separate functional areas depending on the distribution of the MEP lamella, as shown in **Figure 4** and **Table 1**. A muscle in a traditional electrophysiological examination will be divided into multiple functional areas for a more careful electrophysiological examination. This will help to identify the injured nerve branches more accurately. In a traditional electrophysiological examination, a single muscle is considered as a whole. If the electrode is placed in the unit of the normal MEP lamella, the result may indicate that no problem exists. In fact, such a result only reflects the status of

one in-muscle branch of the nerve. For patients who have problems with the other in-muscle nerve branch of the same muscle, it may not be detected. According to our results, the electrophysiological examination protocol should be done at the lamellar level. Each MEP lamella unit needs to be independently examined according to its distribution, especially for patients with clinical symptoms but negative results of traditional electrophysiological examinations. According to the MEP distribution pattern, intramuscular injection of viral vectors containing therapeutic genes or other active pharmaceutical ingredients could be more precise and effective [51, 52]. Physicians could refer to the information on the localization of MEP zones relative to external anatomical landmarks. With these guidelines, the injection of medical agents can be directed to the areas with the largest concentration of MEPs. As the effect relies on its uptake at the presynaptic membrane of the MEP, the injection should be given into the MEP area. Further studies should be performed to confirm the roles of MEP distribution in muscle movement and neuromuscular signal transmission.

Abbreviations

3DISCO: three-dimensional imaging of solvent-cleared organs; α -BTX: α -bungarotoxin; AChR: acetylcholine receptor; BS: bone surface; CMAP: compound muscle action potential; CUBIC: clear, unobstructed brain imaging cocktails and computational analysis; Di: distal end; DS: dorsal surface; MEP: motor endplate; MGL: gastrocnemius lateralis; MGM: gastrocnemius medialis; MIP: maximum-intensity projection; Pr: proximal end; SeeDB: See Deep Brain; ScaleS: a sorbitol-based Scale; TS: tibial surface.

Supplementary Material

Supplementary materials, figures and video legends.

<http://www.thno.org/v09p0734s1.pdf>

Supplementary video 1.

<http://www.thno.org/v09p0734s2.wmv>

Supplementary video 2.

<http://www.thno.org/v09p0734s3.wmv>

Supplementary video 3.

<http://www.thno.org/v09p0734s4.wmv>

Supplementary video 4.

<http://www.thno.org/v09p0734s5.wmv>

Supplementary video 5.

<http://www.thno.org/v09p0734s6.wmv>

Supplementary video 6.

<http://www.thno.org/v09p0734s7.wmv>

Supplementary video 7.

<http://www.thno.org/v09p0734s8.wmv>

Supplementary video 8.

<http://www.thno.org/v09p0734s9.wmv>

Supplementary video 9.

<http://www.thno.org/v09p0734s10.wmv>

Supplementary video 10.

<http://www.thno.org/v09p0734s11.wmv>

Supplementary video 11.

<http://www.thno.org/v09p0734s12.wmv>

Supplementary video 12.

<http://www.thno.org/v09p0734s13.wmv>

Acknowledgments

This work was supported by Chinese National Plan on Key Basic Research Project (Grant No. 2014CB542200), the National Natural Science Foundation of China (Grant Nos. 61860206009, 91749209, 81870934, 31571002, 31471144, 81701354), the Science Fund for Creative Research Group of China (Grant No. 61721092), the Fundamental Research Funds for the Central Universities, HUST (No. 2018KFYXKJC 026), and the Project funded by China Postdoctoral Science Foundation (Grant Nos. 2017M612463, 2018T110772), the Director Fund of WNLO. We thank Shaoqun Zeng, Tonghui Xu, Zhihong Zhang, Peng Fei, Guanxin Shen, and Xiaochuan Wang for their helpful discussion and Tingwei Quan for suggestions on data processing. We also thank the Optical Bioimaging Core Facility of WNLO-HUST for their support in data acquisition.

Competing Interests

The authors have declared that no competing interest exists.

References

- Sanes JR, Lichtman JW. Development of the vertebrate neuromuscular junction. *Annu Rev Neurosci.* 1999; 22: 389-442.
- Pratt SJ, Shah SB, Ward CW, Inacio MP, Stains JP, Lovering RM. Effects of in vivo injury on the neuromuscular junction in healthy and dystrophic muscles. *J Physiol.* 2013; 591: 559-70.
- Prodanov D, Thil MA, Marani E, Delbeke J, Holsheimer J. Three-dimensional topography of the motor endplates of the rat gastrocnemius muscle. *Muscle Nerve.* 2005; 32: 292-302.
- Mohan R, Tosolini AP, Morris R. Segmental distribution of the motor neuron columns that supply the rat hindlimb: a muscle/motor neuron tract-tracing analysis targeting the motor end plates. *Neuroscience.* 2015; 307: 98-108.
- Greising SM, Stowe JM, Sieck GC, Mantilla CB. Role of TrkB kinase activity in aging diaphragm neuromuscular junctions. *Exp Gerontol.* 2015; 72: 184-91.
- Macpherson PC, Farshi P, Goldman D. Dach2-Hdac9 signaling regulates reinnervation of muscle endplates. *Development.* 2015; 142: 4038-48.
- Sakuma M, Gorski G, Sheu SH, Lee S, Barrett LB, Singh B, et al. Lack of motor recovery after prolonged denervation of the neuromuscular junction is not due to regenerative failure. *Eur J Neurosci.* 2016; 43: 451-62.
- Savica R, Grossardt BR, Bower JH, Klassen BT, Matsumoto JY. Clinical failure of botulinum toxin A in movement disorders. *Parkinsonism Relat Disord.* 2012; 18: 73-5.
- Orsini M, Leite MA, Chung TM, Bocca W, de Souza JA, de Souza OG, et al. Botulinum neurotoxin type A in neurology: update. *Neurol Int.* 2015; 7: 5886.
- Ovsepian SV, Bodeker M, O'Leary VB, Lawrence GW, Oliver Dolly J. Internalization and retrograde axonal trafficking of tetanus toxin in motor neurons and trans-synaptic propagation at central synapses exceed those of its C-terminal-binding fragments. *Brain Struct Funct.* 2015; 220: 1825-38.
- Wu C, Xue F, Chang W, Lian Y, Zheng Y, Xie N, et al. Botulinum toxin type A with or without needle electromyographic guidance in patients with cervical dystonia. *Springerplus.* 2016; 5: 1292.
- Straka T, Vita V, Prokshi K, Horner SJ, Khan MM, Pirazzini M, et al. Postnatal development and distribution of sympathetic innervation in mouse skeletal muscle. *Int J Mol Sci.* 2018; 19: 1935.
- Mu L, Chen J, Li J, Nyirenda T, Fowkes M, Sobotka S. Immunohistochemical detection of motor endplates in the long-term denervated muscle. *J Reconstr Microsurg.* 2018; 34: 348-58.
- Thomson SR, Nahon JE, Mutsaers CA, Thomson D, Hamilton G, Parson SH, et al. Morphological characteristics of motor neurons do not determine their relative susceptibility to degeneration in a mouse model of severe spinal muscular atrophy. *PLoS One.* 2012; 7: e52605.
- Tuszynski MH, Steward O. Concepts and methods for the study of axonal regeneration in the CNS. *Neuron.* 2012; 74: 777-91.
- Zipfel WR, Williams RM, Webb WW. Nonlinear magic: multiphoton microscopy in the biosciences. *Nat Biotechnol.* 2003; 21: 1369-77.
- Helmchen F, Denk W. Deep tissue two-photon microscopy. *Nat Methods.* 2005; 2: 932-40.
- Conchello JA, Lichtman JW. Optical sectioning microscopy. *Nat Methods.* 2006; 2: 920-31.
- Stefaniuk M, Gualda EJ, Pawlowska M, Legutko D, Matryba P, Koza P, et al. Light-sheet microscopy imaging of a whole cleared rat brain with Thy1-GFP transgene. *Sci Rep.* 2016; 6: 28209.
- Dotz H-U, Leischner U, Schierloh A, Jahrling N, Mauch CP, Deininger K, et al. Ultramicroscopy: three-dimensional visualization of neuronal networks in the whole mouse brain. *Nat Methods.* 2007; 4: 331-6.
- Tuchin VV. *Optical Clearing of Tissues and Blood.* Bellingham, WA: SPIE Press; 2006.
- Zhu D, Larin KV, Luo Q, Tuchin VV. Recent progress in tissue optical clearing. *Laser Photonics Rev.* 2013; 7: 732-57.
- Yu T, Qi Y, Gong H, Luo Q, Zhu D. Optical clearing for multiscale biological tissues. *J Biophotonics.* 2018; 11: e201700187.
- Ke MT, Fujimoto S, Imai T. SeeDB: a simple and morphology-preserving optical clearing agent for neuronal circuit reconstruction. *Nat Neurosci.* 2013; 16: 1154-61.
- Hama H, Hioki H, Namiki K, Hoshida T, Kurokawa H, Ishidate F, et al. ScaleS: an optical clearing palette for biological imaging. *Nat Neurosci.* 2015; 18: 1518-29.
- Erturk A, Becker K, Jahrling N, Mauch CP, Hojer CD, Egen JG, et al. Three-dimensional imaging of solvent-cleared organs using 3DISCO. *Nat Protoc.* 2012; 7: 1983-95.
- Susaki EA, Tainaka K, Perrin D, Yukinaga H, Kuno A, Ueda HR. Advanced CUBIC protocols for whole-brain and whole-body clearing and imaging. *Nat Protoc.* 2015; 10: 1709-27.
- Tomer R, Ye L, Hsueh B, Deisseroth K. Advanced CLARITY for rapid and high-resolution imaging of intact tissues. *Nat Protoc.* 2014; 9: 1682-97.
- Hou B, Zhang D, Zhao S, Wei M, Yang Z, Wang S, et al. Scalable and Dil-compatible optical clearance of the mammalian brain. *Front Neuroanat.* 2015; 9: 1-19.
- Treweek JB, Chan KY, Flytzanis NC, Yang B, Deverman BE, Greenbaum A, et al. Whole-body tissue stabilization and selective extractions via tissue-hydrogel hybrids for high-resolution intact circuit mapping and phenotyping. *Nat Protoc.* 2015; 10: 1860-96.
- Greenbaum A, Chan KY, Dobrev T, Brown D, Balani DH, Boyce R, et al. Bone CLARITY: clearing, imaging, and computational analysis of osteoprogenitors within intact bone marrow. *Sci Transl Med.* 2017; 9: eaah6518.
- Murakami TC, Mano T, Saikawa S, Horiguchi SA, Shigeta D, Baba K, et al. A three-dimensional single-cell-resolution whole-brain atlas using CUBIC-X expansion microscopy and tissue clearing. *Nat Neurosci.* 2018; 21: 625-37.
- Pan CC, Cai RY, Quacquarelli FP, Ghasemigharagoz A, Loubopoulos A, Matryba P, et al. Shrinkage-mediated imaging of entire organs and organisms using uDISCO. *Nat Methods.* 2016; 13: 859-67.
- Jing D, Zhang S, Luo W, Gao X, Men Y, Ma C, et al. Tissue clearing of both hard and soft tissue organs with the PEGASOS method. *Cell Res.* 2018; 28: 803-818.
- Qi Y, Yu T, Xu J, Wan P, Ma Y, Zhu J, et al. FDISCO: advanced solvent-based clearing method for imaging whole organs. *Sci Adv.* 2019; 5: eaau8355.

36. Panagopoulos GN, Megaloikononimos PD, Mavrogenis AF. The present and future for peripheral nerve regeneration. *Orthopedics*. 2017; 40: e141-e56.
37. Kullmann FA, Chet de Groat W, Artim DE. Chapter 35 - Bungarotoxins. In: Jankovic J, Albanese A, Atassi MZ, Dolly JO, Hallett M, Mayer NH, editors. *Botulinum Toxin*. Philadelphia: W.B. Saunders; 2009: 425-45.
38. Chen W, Yu T, Chen B, Qi Y, Zhang P, Zhu D, et al. In vivo injection of alpha-bungarotoxin to improve the efficiency of motor endplate labeling. *Brain Behav*. 2016; 6: e00468.
39. Aquilonius SM, Askmark H, Gillberg PG, Nandedkar S, Olsson Y, Stalberg E. Topographical localization of motor endplates in cryosections of whole human muscles. *Muscle Nerve*. 1984; 7: 287-93.
40. Becker K, Jahrling N, Kramer ER, Schnorrer F, Dodt HU. Ultramicroscopy: 3D reconstruction of large microscopical specimens. *J Biophotonics*. 2008; 1: 36-42.
41. Erturk A, Mauch CP, Hellal F, Forstner F, Keck T, Becker K, et al. Three-dimensional imaging of the unsectioned adult spinal cord to assess axon regeneration and glial responses after injury. *Nat Med*. 2011; 18: 166-71.
42. Coers C, Durand J. Distribution of cup-shaped cholinesterase apparatus in various striated muscles. *Arch Biol (Liege)*. 1957; 68: 209-215.
43. Christensen E. Topography of terminal motor innervation in striated muscles from stillborn infants. *Am J Phys Med*. 1959; 38: 65-78.
44. Akaaboune M, Culican SM, Turney SG, Lichtman JW. Rapid and reversible effects of activity on acetylcholine receptor density at the neuromuscular junction in vivo. *Science*. 1999; 286: 503-507.
45. Edström L, Kugelberg E. Histochemical composition, distribution of fibers and fatigability of single motor units. Anterior tibial muscle of the rat. *J Neurol Neurosurg Psychiatry*. 1968; 31: 424-33.
46. Larsson L, Edström L, Lindegren B, Gorza L, Schiaffino S. MHC composition and enzyme-histochemical and physiological properties of a novel fast-twitch motor unit type. *Am J Physiol*. 1991; 261: C93.
47. Kugelberg E, Edström L, Abbruzzese M. Mapping of motor units in experimentally reinnervated rat muscle. *J Neurol Neurosurg Psychiatry*. 1970; 33: 319-29.
48. Mu L, Sobotka S, Su H. Nerve-muscle-endplate band grafting: a new technique for muscle reinnervation. *Neurosurgery*. 2011; 69: 208-24.
49. Sobotka S, Mu L. Comparison of muscle force after immediate and delayed reinnervation using nerve-muscle-endplate band grafting. *J Surg Res*. 2013; 179: e117-26.
50. Sobotka S, Mu L. Muscle reinnervation with nerve-muscle-endplate band grafting technique: correlation between force recovery and axonal regeneration. *J Surg Res*. 2015; 195: 144-51.
51. Tosolini AP, Mohan R, Morris R. Targeting the full length of the motor end plate regions in the mouse forelimb increases the uptake of fluoro-gold into corresponding spinal cord motor neurons. *Front Neurol*. 2013; 4: 58.
52. Tosolini AP, Morris R. Spatial characterization of the motor neuron columns supplying the rat forelimb. *Neuroscience*. 2012; 200: 19-30.